JGR Atmospheres

Turbulent Heat Exchange Over Polar Leads Revisited: A Large Eddy Simulation Study

M. Gryschka[1] ![ORCID], V. M. Gryanik[2], C. Lüpkes[3] ![ORCID], Z. Mostafa[1], M. Sühring[1], B. Witha[4], and S. Raasch[1] ![ORCID]

[1]Institute of Meteorology and Climatology, Leibniz University Hannover, Hannover, Germany, [2]A.M. Obukhov Institute for Atmospheric Physics, Russian Academy of Sciences, Moscow, Russia, [3]Alfred Wegener Institute for Polar and Marine Research, Bremerhaven, Germany, [4]Energy & Meteo Systems GmbH, Oldenburg, Germany

Abstract Sea ice leads play an important role in energy exchange between the ocean and atmosphere in polar regions, and therefore must be considered in weather and climate models. As sea ice leads are not explicitly resolved in such models, lead-averaged surface heat flux is of considerable interest for the parameterization of energy exchange. Measurements and numerical studies have established that the lead-averaged surface heat flux depends not only on meteorological parameters, but also on lead width. Nonetheless, few studies to date have investigated the dependency of surface heat flux on lead width. Most findings on that dependency are based on observations with lead widths smaller than a few hundred meters, but leads can have widths from a few meters to several kilometers. In this parameter study, we present the results of three series of large-eddy simulations of turbulent exchange processes above leads. We varied the lead width and air temperature, as well as the roughness length. As this study focused on conditions without background wind, ice-breeze circulation occurred, and was the main driver of the adjustment of surface heat flux. A previous large-eddy simulation study with uncommonly large roughness length found that lead-averaged surface heat flux exhibited a distinct maximum at lead widths of about 3 km, while our results show the largest heat fluxes for the smallest leads simulated (lead width of 50 m). At more realistic roughness lengths, we observed monotonously increasing heat fluxes with increasing lead width. Further, new scaling laws for the ice-breeze circulation are proposed.

Plain Language Summary In polar sea ice, often channel-like openings appear due to ocean and atmosphere currents. These openings are like open windows, where huge amount of heat is transported from ocean to atmosphere. The width of the leads range from a few meters up to more than 10 km. Leads cover only a small area of the polar sea ice, but play an important role in the climate system. Generally, the amount of heat transport depends on wind speed and temperature of air and water. Further, measurements and computational model studies have indicated, that the efficiency of heat transport depends strongly on the width of a lead. Nonetheless, few studies to date have investigated the dependency on lead width. Most findings on that are based on observations for leads smaller than a few hundred meters. In this study, we present results of computer simulations with a so-called large eddy simulation model, which captures the small scale turbulent processes explicitly. We varied the lead width from 50 m to 25 km for the special meteorological conditions without background wind and found remarkably different results compared to a former study on that topic with same type of computational model.

1. Introduction

An important feature of polar sea ice is the presence of leads, the characteristics of which have been described by several authors, and most recently by Michaelis et al. (2020), Michaelis et al. (2021), and Michaelis and Lüpkes (2022). In the following, we summarize their introductory reviews, as well as that of Tetzlaff et al. (2015), and also consider further literature that is relevant to our work. Leads are openings in sea ice that form due to divergence or shear in ice drifts caused by wind or ocean currents. Leads exhibit a channel-like shape, with widths from a few meters to several kilometers and lengths of a few kilometers to several hundred kilometers (Barry et al., 1993), as shown in numerous satellite images (e.g., Figure 1). Leads contribute significantly to the formation of ice (Eisen & Kottmeier, 2000) and bottom water (Midttun, 1985). Although leads account for a small amount of total ice coverage in polar regions (e.g., Lindsay & Rothrock, 1995; Miles & Barry, 1998), they play an important role in the energy balance. For example, Eisen and Kottmeier (2000) found that leads in the western Weddell Sea contribute up to 70% of net energy transfer into the atmosphere, with net heat flux

Figure 1. Leads in the Weddell Sea (Terra Modis image from 19 August 2017). The image shows an area of 150×150 km². Source: NASA worldview, https://worldview.earthdata.nasa.gov.

increasing from approximately 12 to 40 W m⁻² at the surface when the areal fraction covered by leads was considered. Accordingly, individual leads had (sensible) surface heat fluxes of several 100 W m⁻² in experimental studies (e.g., Andreas et al., 1979; Ruffieux et al., 1995; Tetzlaff et al., 2015). Recent studies (Li, Krueger, Strong, & Mace, 2020; Li, Krueger, Strong, Mace, & Benson, 2020) using satellite- and surface-based observations found fewer boundary layer cloud occurrence in higher lead fractions periods. Three-dimensional cloud resolving simulations (Li, Krueger, Strong, Mace, & Benson, 2020) indicate that these counterintuitive results can be explained by mostly newly frozen leads which exhibits high sensible heat fluxes but low latent heat fluxes. The reduced cloud occurrence in turn decreases downwelling infrared flux and accelerates the freezing of sea ice (Li, Krueger, Strong, Mace, & Benson, 2020).

Using a single-column model, Lüpkes, Gryanik et al. (2008) and Lüpkes, Vihma, et al. (2008) demonstrated that a change of 1% in the lead fraction may cause changes in the near-surface temperature of several Kelvin across a large area surrounding the leads, depending on the meteorological situation. At the global scale, Ledley (1988) studied the impact of leads on climate using a coupled energy balance climate–sea ice model. Their results indicated a significant increase in annual zonally averaged temperature of 1.0 K in polar regions, and an increase in the tropics of 0.2 K when the minimum lead fraction was increased from 1.1% to 4.3%. Using a general circulation model, Grötzner et al. (1996) found that considering subgrid-scale sea-ice inhomogeneities (rather than defining model grid cells as either fully covered with ice or free of ice) leads to significant warming and moistening of the polar troposphere, which impacts atmospheric circulation at high and middle latitudes. Using data from measurement campaigns, Andreas and Cash (1999) and Andreas and Murphy (1986) empirically determined bulk transfer coefficients for heat and momentum as a function of the lead width λ and Obukhov length. They found that the transfer coefficient for heat and surface heat flux per unit area increase significantly with decreasing lead width at widths smaller than approximately 200 m, while the transfer coefficient for wider leads remains constant, with values typical for the open ocean. Similar results were obtained by Alam and Curry (1997) using a theoretical approach based on Monin–Obukhov similarity theory and the surface renewal theory (Brutsaert, 1975). For leads wider than 1,000 m Michaelis and Lüpkes (2022) used a non-eddy-resolving microscale model and found that surface heat flux per unit area increased with increasing lead width.

Several studies have demonstrated a power law distribution of lead width (e.g., Lindsay & Rothrock, 1995; Wadhams et al., 1985), and the elevated heat transfer capacity of small leads is thus of particular importance. Therefore, Marcq and Weiss (2012) applied the methods of Andreas and Murphy (1986), Andreas and Cash (1999) and Alam and Curry (1997) to calculate areal average heat flux while considering the lead width distribution derived from a satellite image obtained over an area of 60×66 km² under various assumed meteorological conditions. Using that method, they found significantly larger fluxes (up to 55%) compared to the situation in which the open water fraction constitutes a single large lead. To our knowledge, neither the non-linear dependence of surface heat flux on lead width nor the power law distribution of lead width has been considered in climate models.

Due to the large impact of sea-ice leads on atmosphere–ocean heat exchange and its importance for the global climate system (e.g., Hanna, 1996), improving the parameterization of climate models for sea ice surfaces with leads is worthwhile. Knowledge of turbulent exchange processes in the environment around leads derived from observations remains limited to specific cases, and data as a continuous function of lead width are not yet available. Therefore, to elucidate these physical processes, explicit simulation of turbulent processes in the lead environment is necessary, and has been conducted using large-eddy simulation (LES) models. In the first LES studies on this topic by Glendening and Burk (1992) and Glendening (1995), the basic plume structure that develops when the air temperature is much lower than the surface temperature of leads was discussed for a lead width of 200 m. In that study, the plume heights associated with different wind directions were analyzed, which aligned with the analytical function obtained from dimensional arguments, but did not fit the theoretically obtained function of Serreze et al. (1992). Furthermore, they investigated the vertical distribution of horizontally integrated

heat flux and found an exponential decrease with height. For a similar case of a 200 m-wide-lead and weak background wind of 2.5 m/s, Weinbrecht and Raasch (2001) found that a resolution of at least 2 m horizontally and 1 m vertically was necessary to sufficiently resolve processes above the lead. They found that increasing wind speed required a further increase in the resolution to ensure that turbulence above the lead is resolved. Lüpkes, Gryanik, et al. (2008) and Lüpkes, Vihma, et al. (2008) simulated convection above leads using LES and a non-eddy-resolving microscale model for comparison, while varying wind speed and upstream air temperature. They developed a new parameterization for 1 km-wide leads in microscale models that resolve the mean flow structures above the lead, but not the turbulence. That parameterization was improved by Michaelis et al. (2020) to account for variable lead width and atmospheric conditions, and validation against measurements was reported in Michaelis et al. (2021).

Esau (2007) (hereafter referred to as ES07) conducted the first set of LES for lead widths that varied across a large range of 5 m and 20.5 km. Unlike previous LES studies, meteorological conditions without background wind were investigated. Although such conditions are not predominant in polar regions, ES07 analyzed data from the SHEBA campaign (Uttal et al., 2002) and found that wind speed was less than 2 ms^{-1} on 60 of the 255 days in the SHEBA data set. He found a peak in lead-averaged surface heat flux for lead widths λ_{max} of about 2–4 km, which is approximately five times greater than the result obtained with the same initial meteorological conditions over open water (Figure 4 in ES07). He argued that heat transport via ice-water breeze circulation (IBC) is more effective than heat transport via convection over a homogeneous surface, assigning the former condition to forced convection and the latter to free convection. For leads smaller than λ_{max}, the flow regime is dominated by a single updraft over a lead associated with IBC, while for wider leads several updrafts appear in association with convective cells. For wider leads, the free convection regime dominates, and surface heat flux tends toward open-ocean conditions. Although this concept explains the decrease of heat flux with increasing lead width at $\lambda > \lambda_{max}$, it does not explain the decrease with decreasing lead width at $\lambda < \lambda_{max}$. Actual results obtained for $\lambda < \lambda_{max}$ differ from the findings of studies based on observations (Andreas & Cash, 1999; Andreas & Murphy, 1986), wherein the heat flux increased significantly with decreasing lead width (within the observed range of $7m \leq \lambda \leq 500 m$). That difference provided a starting point for our study, which addresses the following research questions:

- What is the dependency of lead-averaged surface heat flux on lead width under calm background wind conditions, and will it converge toward the value for the open ocean with increasing lead width?
- What explains the discrepancy between the findings of the LES-study ES07 for narrow to wide leads and observational studies on narrow leads by Andreas and Cash (1999) and Andreas and Murphy (1986)?
- How does plume height depend upon lead width under calm background wind conditions, and is an existing scaling law for plume height for lead-parallel background wind appropriate here?
- What is the scaling for the IBC?
- Does the Coriolis force impact convection above wider leads under calm background wind conditions?

To address these questions, we performed three series of LES. First, we used the same meteorological conditions as ES07, but obtained a significantly different result for lead width dependency. These results and the reason, for the discrepancy between our results and those of Esau, are discussed in Section 3.1. As ES07 used unusually large values for roughness length and a relatively small near-surface temperature difference between ice and water, we expanded our study to include more realistic values, which are discussed in Section 3.2.

In the following section, we describe the LES model used in the present study and the simulation conditions for the various experiments.

2. Numerical Experiments and Methods

2.1. LES Model

We used PALM model system 21.10 (Maronga et al., 2015, 2020). PALM has been used in several studies of polar boundary layers over heterogeneously heated surfaces (e.g., Gryschka et al., 2008, 2014; Michaelis et al., 2020; Sühring et al., 2014). We operated PALM in LES mode, wherein the non-hydrostatic, filtered, incompressible Navier–Stokes equations in Boussinesq-approximated form are solved along with a subgrid-scale model based on 1.5-order closure after Deardorff (1980). Monin–Obukhov similarity theory (MOST) was applied between the surface and first vertical grid level. Lateral periodic boundary conditions were used. Advection was treated with a fifth-order advection scheme (Wicker & Skamarock, 2002), and time stepping with a third-order Runge–Kutta scheme (Williamson, 1980).

2.2. Setup

We conducted three series of simulations SA, SB, and SC, differing in roughness length and the temperatures of the initial air mass and ice surface. Each series consists of 10 simulations with the same meteorological conditions and a lead width λ varying between 50 m and 25 km for the first 9 simulations. The last simulation in each series was conducted with an open water surface applied across the whole model domain. A straight lead was aligned along the y-direction in the center ($x = 0$) of the model domain. As we used cyclic boundary conditions for the model domain in both lateral directions, the length of the lead is endless in the y-direction and the lead occurs periodically in the x-direction. The width of the model domain was set to 10 times the lead width ($L_x = 10\lambda$). In that manner, quasi-stationarity in the development of the surface heat flux was achieved before the periodically recurring leads could influence each other (see discussion in Section 3.1.2), and the effect of a single lead could thus be investigated. For lead widths of up to 2,500 m, the model domain length along y was set to $L_y = 1.3\lambda$, while for wider leads it was kept constant at $L_y = 2,560$ m. This scaling scheme guaranteed that the largest convective eddies above the lead could expand in the y-direction without being limited by the cyclic boundary conditions; we found that the length scales of the largest eddies in the y-direction are always smaller than the lead width and maximum plume height (see Section 3.4). The height of the model domain L_z for each setup was several times larger than the expected plume height. This was achieved by conducting the simulations in order from the narrowest to the widest lead, while we gradually increased the domain height depending on the plume height obtained from the previous simulation. In the upper third of the model domain (far enough from the plume), vertical grid stretching was applied. The resolution of the isotropic model grid, Δx_i, was selected such that the lead width was resolved with at least 200 grid points, but never exceeded 20 m. Those limits should guarantee that the smallest relevant scales of the turbulent structures driving turbulent transport are resolved; these structures are assumed to be controlled by lead width for smaller leads, and by the size of the convection cells for larger leads. Further, the high resolution (in all three dimensions) should guarantee that uncertainties by MOST, which strictly speaking is only applicable for homogeneous surface, are minimized near the ice edges. At the end of Section 3.1.1 this point will be further discussed in conjunction with simulation results.

For the first series of simulations, SA, we used the same initial meteorological and surface boundary conditions as ES07 described in his experiments 1 to 43. Initially, a stably stratified air mass with a vertical gradient of potential temperature of $\partial_z \theta = 9.7$ K km^{-1} was prescribed, in which the near-surface value matched the temperature of ice $T_i = 263.35$ K across the whole model domain. The water temperature was defined as $T_w = 271.35$ K. The roughness length (for momentum and heat) for ice was set to $z_{0_i} = 0.1$m and that for water to $z_{0_w} = 0.01$m. In accordance with most of the experiments in ES07, we neglected Coriolis force for the sake of comparability; 2 out of 43 experiments of ES07 were conducted with Coriolis force, but no significant differences were found. The effect of Coriolis force was investigated within series SC (see below).

As the values for roughness length for water and ice were much higher in these experiments than those commonly used for such analyses, we repeated the simulations in series SB for $z_{0_i} = 10^{-3}$ m and $z_{0_w} = 10^{-4}$ m, which is in the range used in most numerical studies of convection above leads (e.g., Glendening & Burk, 1992; Lüpkes, Gryanik, et al., 2008; Lüpkes, Vihma, et al., 2008; Zulauf & Krueger, 2003).

The difference in surface temperatures ΔT_s between water and ice of 8 K prescribed by ES07 is moderate and typical for mid-spring, but not for the period of late autumn to early spring. Due to the smaller (but more realistic) roughness length used in SB, this moderate temperature difference leads to small heat fluxes of less than 30 W/m². Thus, for series SC we increased ΔT_s sharply to 25 K, thereby setting the temperature of ice to $T_i = 246.35$ K. As we applied the same vertical temperature gradient as in SA/SB, here the air mass initially is 17 K colder than in SA/SB. All other parameters were kept the same as in SB. The simulations for 10- and 25 km-wide leads were conducted a second time considering Coriolis force for a geographical latitude of 79° north, as the Rossby number calculated from the mean velocity of IBC implies a strong impact of the Coriolis force on mean flow (see discussion in Section 3.5).

The simulation time varied between 1 and 25 hr, and consistently exceeded the time when quasi-stationarity is reached (refereed to as τ) by a factor of at least 2. All parameters that differ among series SA, SB, and SC are listed in Table 1. The parameters that varied within each series and τ are summarized in Table 2. The determination of τ is described in Section 3.1.2.

We like to mention that in ES07 leads even narrower than 50 m were taken into account in contrast to our study. The reason for our choice to start at 50 m are as follows: We claim to resolve the leads with at least 200 grid points

Table 1
Values Used for the Roughness Lengths of Ice(z_{0i}) and Water (z_{0w}), Surface Temperatures of Water (T_w) and Ice (T_i) and Surface Temperature Difference $\Delta T_s = T_w - T_i$ for the Simulation Series SA, SB, and SC

Series	z_{0i} (m)	z_{0w} (m)	T_w (K)	T_i (K)	ΔT_s (K)
SA	10^{-1}	10^{-2}	271.35	263.35	8
SB	10^{-3}	10^{-4}	271.35	263.35	8
SC	10^{-3}	10^{-4}	271.35	246.35	25

(to ensure the turbulence is mainly resolved above the lead). For example, in case of a 10 m wide lead, the resolution would result in $\Delta x_i = 5$ cm. Beside the large computational time which would be needed for such cases, in the study SA the height of the first numerical grid point above the surface would be smaller than the roughness length, which would be in conflict with the surface boundary condition, where MOST is applied between surface and first grid level. In ES07, the smallest lead ($\lambda = 5$ m) was only resolved with five grid point.

2.3. Statistical Methods

Before presenting the results, we should explain how turbulent quantities are defined in this analysis and what types of averaging are utilized. As the problem considered here is statistically homogenous in the *y*-direction, we defined the resolved turbulent fluctuation of a quantity Ψ as

$$\Psi' = \Psi - \langle \Psi \rangle_y, \tag{1}$$

with $\langle \Psi \rangle_y$ as the average of Ψ along *y*. Our analysis focuses on the vertical turbulent heat flux *F*, which after averaging along *y* can be expressed as:

$$\langle F \rangle_y = \langle w'\theta' \rangle_y + \langle F_s \rangle_y. \tag{2}$$

The first term on the right-hand side is the resolved turbulent heat flux, with w' and θ' representing the turbulent fluctuations defined by Equation 1 for vertical velocity and potential temperature, respectively. The second term is the subgrid-scale turbulent heat flux, which is obtained from the subgrid-scale parameterization of the LES model.

Aside from the average value along *y*, several quantities of Ψ are horizontally averaged across the lead area, designated $\langle \Psi \rangle$.

Table 2
Variable Parameters Used for the Series of Simulations SA, SB, and SC and the Time When Quasi-Stationarity Was Reached, τ

Simulation	λ (m)	L_x (m)	L_y (m)	L_z (m)	$\lambda/\Delta x_i$	Δx_i (m)	τ (min) SA	SB	SC
SA/SB/SC-01	50	512	64	872	200	0.25	5	8	5
SA/SB/SC-02	100	1,024	128	1,135	200	0.50	7	12	7
SA/SB/SC-03	250	2,560	320	1,013	200	1.25	10	28	12
SA/SB/SC-04	500	5,120	640	1,436	200	2.50	15	45	25
SA/SB/SC-05	1,000	10,240	1,280	2,611	200	5.00	30	75	45
SA/SB/SC-06	2,500	25,600	2,560	2,611	500	5.00	60	165	90
SA/SB/SC-07	5,000	51,200	2,560	2,611	1,000	5.00	105	250	135
SA/SB/SC-08	10,000	102,400	2,560	2,294	1,000	10.00	165	450	285
SC-08C	10,000	102,400	2,560	2,294	1,000	10.00	–	–	285
SA/SB/SC-09	25,000	256,000	2,560	2,260	1,250	20.00	345	915	435
SC-09C	25,000	256,000	2,560	2,260	1,250	20.00	–	–	435
SA/SB/SC-10	∞	5,120	5,120	2,580	–	10.00	5–345	8–915	5–435

Note. In case of SA/SB/SC-10 τ does not mark quasi-stationarity, but the time analysis was done (see Section 3.3). Simulations SC-08C and SC-09C were conducted with Coriolis force at a latitude of 79° north.

Notably, some quantities shown in the figures are also temporally averaged. For simplicity, we did not indicate such averaging, but note it in the captions of the appropriate figures.

3. Results

3.1. Results for SA and Comparison With ES07

Before discussing the dependency of lead-averaged surface heat flux on lead width in experiment SA, we focus on a 5 km-wide lead (SA-07) in the next subsection, and discuss the distribution of near-surface heat flux associated with IBC above the lead and other factors near the surface.

3.1.1. Detailed Analysis of One Lead-Scenario

As shown in Figure 2a for a simulation time of 1 hr, IBC develops on both sides of the lead, while the mean wind is almost zero between those IBCs, indicating that free convection dominates that area. This finding is supported by the cellular structure of the instantaneous vertical velocity, which is typical for free convection, as shown in the overlaid x-y cross-section in Figure 2a. The convective plume (area of positive turbulent heat flux) reaches a height h of about 280 m across the whole span, while it is less than 50 m in height in the IBC-dominated region and is capped by an inversion above that height, respectively (the inversion will be discussed at the end of this section together with vertical profiles). In the shallow part of the plume, convection patterns look more streak-like, indicating convection is forced by wind-shear caused by the IBC. For the categorization of the stability of the convective boundary layer (CBL) $-h/L$ is a common parameter, where L is the Obukhov length. The larger the value, the less wind shear drives the convection in the entire CBL. It is well known (e.g., Khanna & Brasseur, 1998; Salesky et al., 2017) that for values larger than about 100 cellular convective patterns appear, while for decreasing values these patterns are increasingly modified by the wind shear (up to streak-like structures or roll convection). We found values around 300 between the IBCs and around 20 in the IBC region, which sustains the classification into the two convection regimes. Under the influence of IBC, the surface heat flux (see gray line in Figure 2c) has its largest values, as cold air is advected from the ice and dynamic mixing is enhanced by IBC. In the free convection regime between the inner edges of the IBC zones, surface heat flux is constant along x at approximately half of the maximum value under IBC.

After 2 hr of simulation (Figure 2b), secondary flow is fully developed, and IBC propagates toward the center of the lead where the rising branches of circulations merge and the maximum plume height (360 m) is achieved. The free convection regime is completely replaced by the forced convection regime of the IBC. The horizontal profile of the surface heat flux $\langle F_0 \rangle_y$ at 2 hr is discussed below in more detail in conjunction with the profiles of the surface layer temperature scale $|\langle \theta_* \rangle_y|$ (absolute value here because θ_* is negative in the convective case), friction velocity $\langle u_* \rangle_y$, potential temperature $\langle \theta \rangle_y$ in the lowest grid level above the surface and velocity $\langle u \rangle_y$ in the lowest four grid levels above the surface (Figures 2c–2g, respectively). Surface heat flux (specifically, the heat flux in the surface layer) can be expressed as

$$F_0 = -u_* \theta_*,\tag{3}$$

where u_* and θ_* can be interpreted as the contributions to heat flux of temperature and velocity fluctuations in the surface layer, respectively. Averaged along y that decomposition can be written as

$$\langle F_0 \rangle_y = -\langle u_* \rangle_y \langle \theta_* \rangle_y - \langle u_*' \theta_*' \rangle_y.\tag{4}$$

The second term on the right-hand side will be neglected in the following qualitative discussion on the horizontal profiles (but it is included in the graph of $\langle F_0 \rangle_y$ in Figure 2c), because it is almost zero under the horizontal branch of the IBC and contribute in the center under the updraft not more than 20%. The heat flux has two distinct maxima of 0.13 K m/s in each half of the lead; one is located directly at the edge and the other at a distance of 0.12λ therefrom (see Figure 2c). From the position of the second maximum, heat flux decreases monotonically to its minimum value of 0.07 K m/s. The maximum at the lead edge is a result of cold air impinging on relatively warm water, leading to a maximum of $|\langle \theta_* \rangle_y|$ (Figure 2d) associated with the large vertical temperature gradient near the surface. Driven by near-surface wind, the air is rapidly warmed by about 2 K across a short fetch of 0.06λ in the first grid level above the surface (Figure 2f), leading to a significant decrease in $|\langle \theta_* \rangle_y|$. Meanwhile, vertical mixing of the horizontal wind $\langle u \rangle_y$ (indicated by the merging of horizontal wind profiles for different grid levels in Figure 2g) leads to a significant increase in wind speed from 1 to 2.5 m/s over a fetch of 0.12λ in the first grid level,
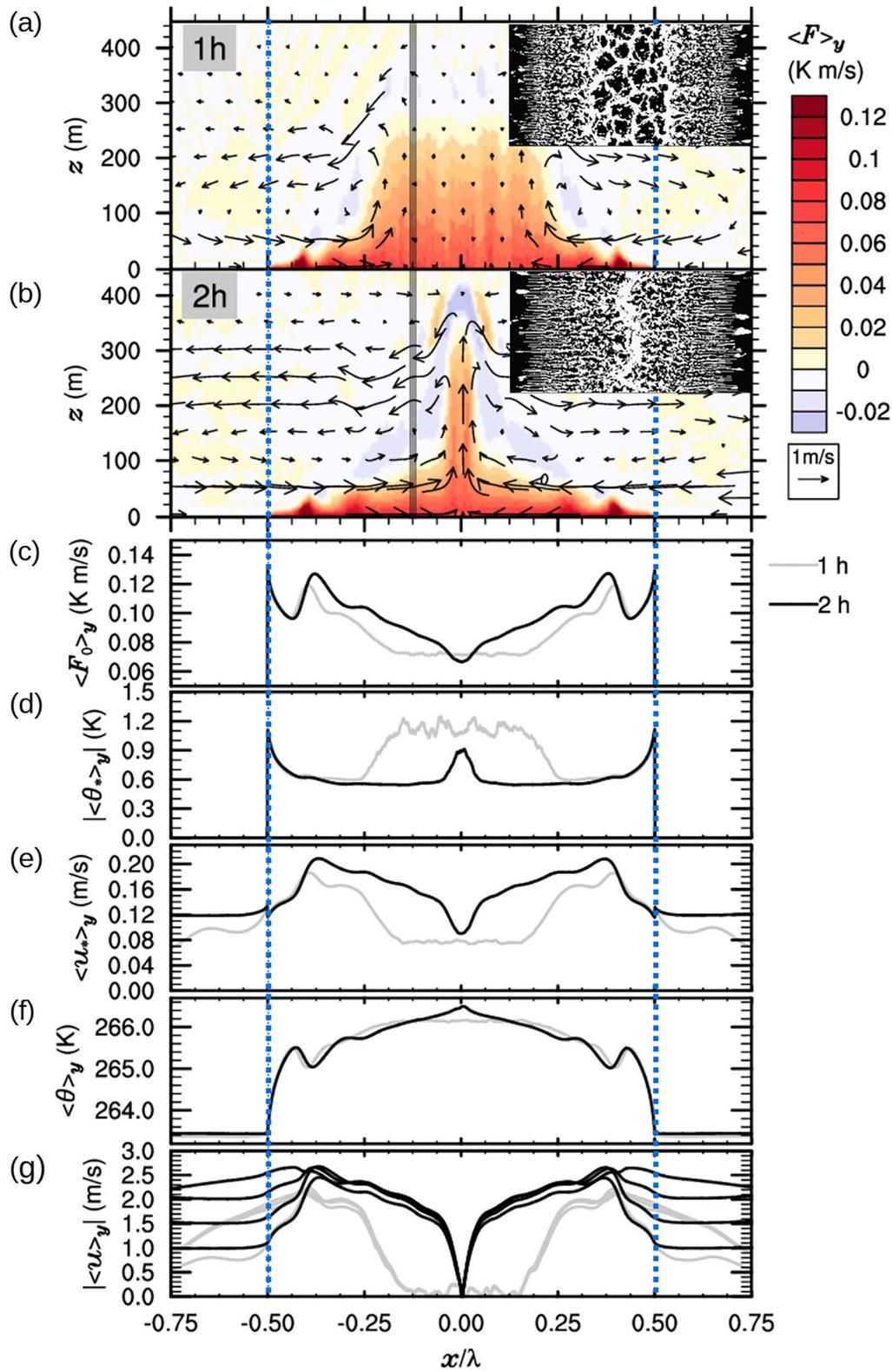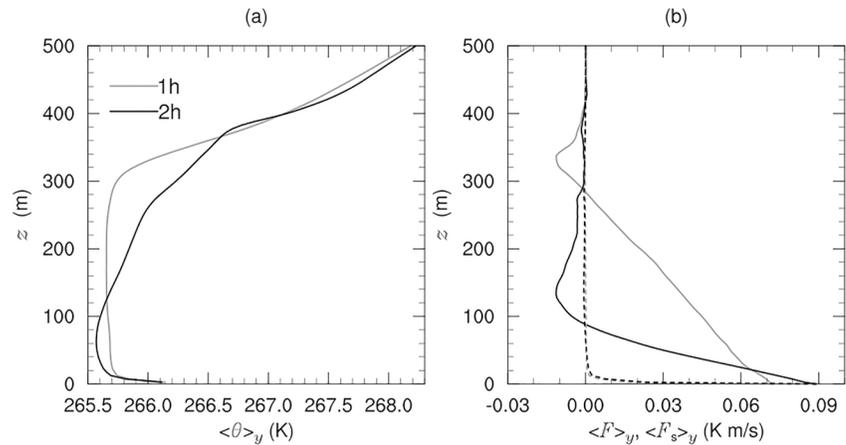
Figure 2.

Figure 3. Vertical profiles of (a) potential temperature θ and (b) turbulent heat flux F (solid lines) and subgrid turbulent heat flux F_s (dashed lines) after 1 and 2 hr of Simulation SA-07 (5 km-lead) at position $x/\lambda = -0, 125$ (marked by the vertical line in Figures 2a and 2b). All values are averaged along y and over 900 s.

which in turn causes an increase of $\langle u_* \rangle_y$ (Figure 2e) that leads to the second maximum of heat flux. Further downstream, surface heat flux decreases monotonically due to convergence of the lower IBC branches at the center of the lead (Figure 2c). In addition, $\langle u_* \rangle_y$ decreases monotonically, while $|\langle \theta_* \rangle_y|$ remains nearly constant (Figures 2d and 2e); this fully explains the decrease of F_0 toward the lead center. In the inner 10% of the lead, $|\langle \theta_* \rangle_y|$ exhibits a local maximum (Figure 2d) due to the major instability in that area, which is offset by an even greater decrease in $\langle u_* \rangle_y$ (Figure 2e) that is accompanied by rapid deceleration of the near-surface wind (Figure 2g). Although the mean horizontal wind is zero at the center, $\langle u_* \rangle_y$ maintains a value that is approximately 50% of its maximum here (Figure 2e). This pattern is caused by the contribution of convective motions to $\langle u_* \rangle_y$, as the average absolute wind speed of convective eddies is much greater than zero (in contrast to the mean wind speed).

For a better understanding of the vertical structure within the developing process of the IBC, Figure 3 shows vertical profiles of potential temperature $\langle \theta \rangle_y$ and turbulent heat flux $\langle F \rangle_y$ at $x/\lambda = -0.125$ (marked by the vertical line in Figure 2). After 1 hr, the position of the profile is just within the free convection regime. Here, the profiles exhibit properties of a typical well mixed CBL capped by an inversion at $z = 300$ m, followed by the free atmosphere at $z = 400$ m. The turbulent heat flux decreases linearly with height with negative values within the capping inversion between $z = 300$ and 400 m and its minimum in between, indicating the entrainment. After 2 hr, the position of the profiles is within the IBC-dominated region. As in the lower branch of the IBC cold air is advected, an internal shallow CBL of 100 m in height has formed. Within that mixed layer the profile of the heat flux also exhibits the typical linear shape for a CBL, but further above it exhibits a relatively broad vertical range of 2 times the internal CBL-height ($z = 100$–300 m) of negative values which does not represent the typical shape for the entrainment zone above a classical CBL. Within that region, the capping inversion is still affected by the downdrafts emerging from the overshooting plume at the plume center, where entrained warm air is transported downward (see discussion on Figure 2 in Sühring et al. (2014)). The temperature profile above the internal CBL is modified not only by the turbulent heat flux, but also by advective processes of the IBC. As the profiles are constant in time from 2 hr on (not shown here), it means that heating/cooling by the turbulent heat flux gradient is balanced with advection of temperature by the IBC.

In Figure 3b additionally vertical profiles of the subgrid turbulent heatflux $\langle F_s \rangle_y$ are shown. As well after 1 hr as after 2 hr at the position, $x/\lambda = -0.125$ it contributes significantly to the turbulent heat flux $\langle F \rangle_y$ only very close to the surface. Generally, above the second grid point, heat flux is resolved by more than 90% in the inner 80% of the lead. Close to the ice edge, the heat flux is dominated by the subgrid scale model (not shown here). Therefore, the peak of the surface heat flux in Figure 2c at the ice edge ($x/\lambda = \pm 0.5$) might be questionable

Figure 2. x-z cross-sections of (a, b) the wind vector (u, w) and turbulent heat flux F, respectively, and horizontal profiles of (c) surface heat flux F_0, (d) potential temperature scale θ_*, (e) friction velocity u_*, (f) potential temperature θ at the lowest grid level ($z = 2.5$ m) and (g) velocities u in the lowest four grid levels ($z = 2.5$, 7.5, 12.5, 17.5 m) after 1 and 2 hr of simulation SA-07 (5 km-lead). All values are averaged along y and over 900 s. Further, in (a) and (b), the horizontal cross-sections covering the area of the lead for instantaneous vertical velocity (vertically averaged over the lowest 100 m) after 1 and 2 hr are overlaid. Black represents downward motion and white indicates upward motion. The center of the lead is defined at $x = 0$ and the vertical dotted blue lines mark the positions of the lead edges. The vertical solid line in (a) and (b) marks the position of the vertical profiles shown in Figure 3.
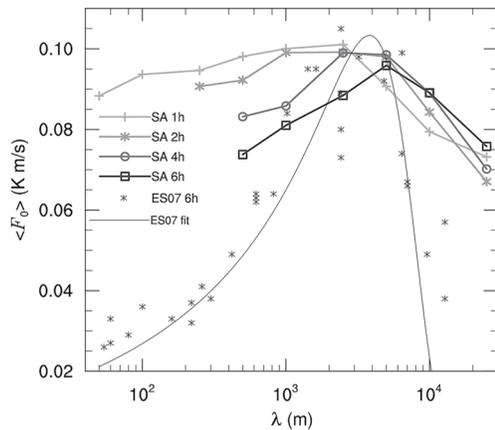
Figure 4. Dependency of lead-averaged surface heat flux on lead width for SA with various simulation times, and for ES07 at 6 hr, along with the proposed fitting function.

(especially in conjunction with MOST, which strictly speaking is only applicable for homogeneous surfaces). But first, we like to mention that we carried out for this case further simulations with lower resolution (half and quarter of SA-07) and found that from the lower to the higher resolution the surface heat flux converges to the shown solution (not shown here). Second, we are mainly interested on the lead averaged surface heat flux in this study and the uncertainty in the exact value at the ice edge will contribute only very little to it. Actually, MOST is widely used in LES studies over heterogeneous surfaces (e.g., Michaelis et al., 2020; Sühring et al., 2014; van Heerwaarden et al., 2014).

3.1.2. Dependency of $\langle F_0 \rangle$ on Lead Width

The main aim of this study is to investigate the dependency of lead-averaged surface heat flux $\langle F_0 \rangle$ on lead width λ. In Figure 4, the results for the simulation chain SA after 1, 2, 4, and 6 hr of integration are shown. Additionally, the results from the experiments in ES07 (6-hr integration time) are shown here, as well as the fitting function proposed by ES07. For all times of SA presented here, heat flux exhibits a maximum at lead widths between 2.5 and 5 km, in accordance with ES07. Nevertheless, the dependency of $\langle F_0 \rangle$ on λ varies markedly over time and does not converge to a final solution. The reason for this variability is that the flows over different lead widths are at different development stages when compared at fixed times. We illustrate this point with Figure 5a, in which $\langle F_0 \rangle$ is plotted against simulation time for SA-04 to SA-09. After the spin-up time (i.e., the time before the first minimum), the lead averaged surface heat flux increases due to the propagation of the IBC to the inner of the lead (under the IBC the surface heat flux is larger than in the free convection regime, as discussed in the last Section 3.1.1). The maximum value (indicated by the crosses) is reached when the inner branches of the IBC merge and quasi-stationarity is reached (referred as τ). Thus, for $\lambda = 5$ km, the maximum appears at 2 hr, which is noted in Section 3.1.1 as the time at which IBC over the lead had fully developed. As shown in Figure 5a τ increases with lead width from a few minutes to several hours. When the simulation time is several times larger than τ, heat fluxes begin to continuously and significantly decrease from their maxima. This pattern is particularly evident for $\lambda = 500$ m (SA-04), where the heat flux decreases by about 30% from its maximum value, from about $t = \tau = 15$ min to $t = 14\tau = 6$ hr. That decrease can be explained as follows: although IBC over water is already fully developed, the branches over ice broaden permanently toward the inner ice region. Due to the lateral cyclic boundary conditions, the branches of both sides of the lead will coincide at some point and then cannot broaden further. Therefore, air within the circulation cell will show continual warming. In other words, warmer air is now advected over the lead, which weakens the surface heat flux. From that time on, the simulation cannot be interpreted as a simulation of a single lead anymore, but instead as an infinite number of leads a certain distance from each other. As the model domain width was always set to 10 times the lead width, the flow over the lead is fully developed before the two branches of the IBC coincide in the inner ice, which guarantees that our results at $t = \tau$ represent the effect of individual leads. Generally, the surface heat fluxes for all simulations did not decrease by more than 3% between $t = \tau$ and $t = 2\tau$. For cases SA-04–SA-09, this pattern is better illustrated by Figure 5b than Figure 5a, where the time axis is normalized to τ. The similarity of the graphs in Figure 5b highlights that τ is an appropriate scale for comparing simulations with different lead widths.
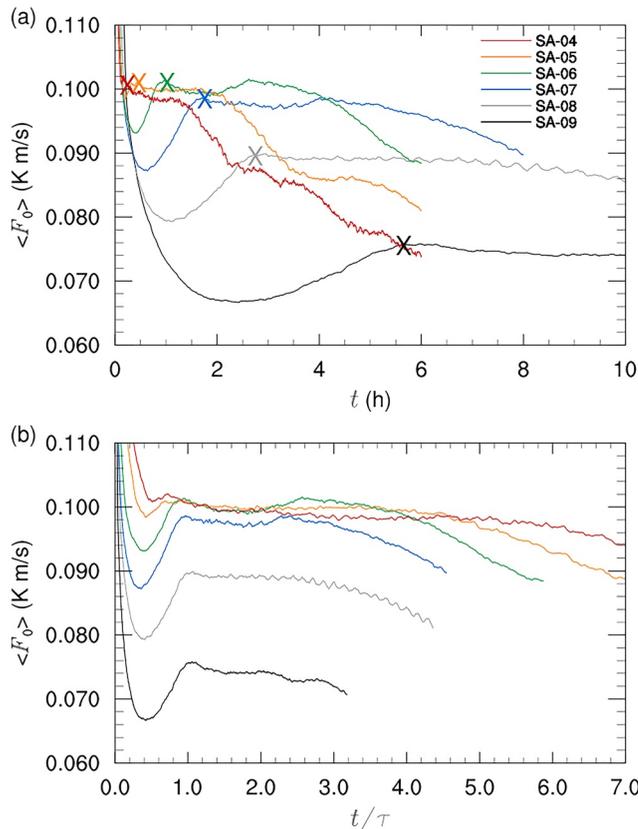

Figure 5. (a) Temporal evolution of lead-averaged surface heat flux $\langle F_0 \rangle$ for simulations SA04–SA09. The crosses mark the time $t = \tau$ for each simulation. (b) Same as (a) but with simulation time t normalized to τ.
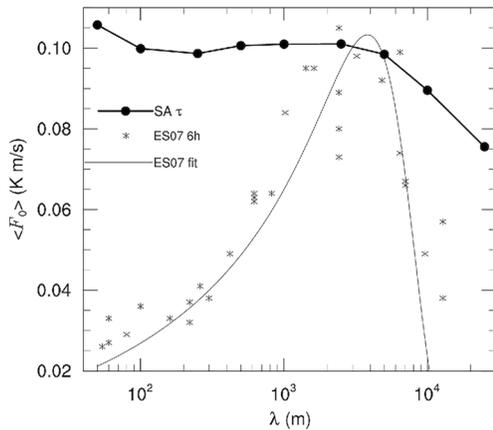
Figure 6. As in Figure 4, but for SA at $t = \tau$.

As in Figure 4, Figure 6 shows the dependency of $\langle F_0 \rangle$ on λ for ES07 at $t = 6$ hr but for SA at $t = \tau(\lambda)$. The largest values of heat flux are associated with the narrowest leads. With increasing lead width, heat flux decreases monotonically to $\lambda = 250$ m, and then remains nearly constant until $\lambda = 2,500$ m before again decreasing monotonically. Overall, heat flux decreases by 30% in the simulated cases, from $\lambda = 50$ m to $\lambda = 25,000$ m. Some differences in the results between ES07 and ours might have been caused by using another LES model than in the study ES07 (LESNIC), but the analysis above suggests that the main differences are due to the following reasons:

1. The analysis time in ES07 was 6 hr for all simulations, and thus was independent of the developmental stage of the flow.
2. The model domain width in ES07 did not scale with lead width; instead, it was arbitrarily selected. For lead widths smaller than a few kilometers, the ratio L_x/λ had values up to 204, while for wider leads it remained less than 10 with a typical value of 2. In other words, the ice-water fraction differed significantly with lead width, which impacted the development of surface heat flux above the lead, as explained in the following paragraphs.
3. The simulations for lead widths smaller than 200 m in ES07 were resolved with fewer than 10 grid points (in x − direction).

Points 1 and 3 may explain why the decreasing lead width from the peak at about $\lambda = 3$ km causes heat flux to decrease significantly, in contrast to SA at $t = \tau$. Although the model domain is rather large compared to the lead width, the analysis time of 6 hr is so long that the warming effect caused by the cyclic boundary conditions is significant. Furthermore, especially for very small leads, the relatively low resolution used may cause underestimation of heat flux. The much smaller heat fluxes obtained for $\lambda > 3$ km may be attributable to points 1 and 2. First, in ES07 at 6 hr, IBC is not fully developed at the center of the lead (see Figure 6 in ES07), which leads to smaller heat flux estimates, as illustrated in Figure 5. Second, for the widest leads, the model domain width is only 2 to 3 times larger than λ. Thus, the warming associated with the cyclic boundary conditions may occur despite IBC not being fully developed over the lead.

Overall, the differences between ES07 and SA can be interpreted as follows: whereas the effect of a single lead was investigated in SA at a stage when IBC was fully developed, the effect of multiple leads (of the same width for each experiment) was included in ES07, but these leads were assessed at different development stages, and with different ice-water fractions at a fixed analysis time.

3.2. Results for SB and SC in Comparison With SA

As noted in Section 2 the roughness length in SA (and ES07) was two orders of magnitude too large to represent the typical conditions around polar leads. Therefore, SB and SC were conducted with more realistic roughness lengths. The circulation features and horizontal profiles of $\langle F_0 \rangle_y$, $\langle \theta_* \rangle_y$, $\langle u_* \rangle_y$, $\langle \theta \rangle_y$ and $\langle u \rangle_y$ are similar to those shown in Figure 2. Figure 7 shows various lead-averaged quantities as a function of lead width for SA, SB, and SC at $t = \tau(\lambda)$. As shown in Figure 7a, the shorter roughness length in SB leads to values of $\langle F_0 \rangle$ that are approximately 10%–25% of those in SA at various lead widths.

With a larger (and more typical for wintertime) temperature difference between ice and water (25 K rather than 8 K), the order of heat flux values in SC is the same as that of SA. Compared to SA, heat fluxes increased significantly with lead width in both SB and SC. For better comparability, the heat fluxes in Figure 7d are normalized to the values for the smallest lead width of each case. While the heat flux in SA decreases by 30% from the smallest to the largest lead (as discussed in Section 3.1.2), the corresponding increases are nearly 80% in SB and 140% in SC.

To discuss these differences in behavior with decomposition of the heat flux in Equation 3, the dependencies of $|\langle \theta_* \rangle|$ and $\langle u_* \rangle$ on lead width are plotted in Figures 7b and 7c, and are shown normalized to the values for the smallest lead width in Figures 7e and 7f, respectively. First, for all cases, $|\langle \theta_* \rangle|$ decreases monotonically, while $\langle u_* \rangle$ increases monotonically with lead width. This finding implies competition between at least two drivers. One process causing negative feedback is the fetch-dependent warming effect (FDW effect). Wider leads cause more warming of near-surface air on its way to the center, leading to a smaller near-surface vertical temperature gradient (averaged
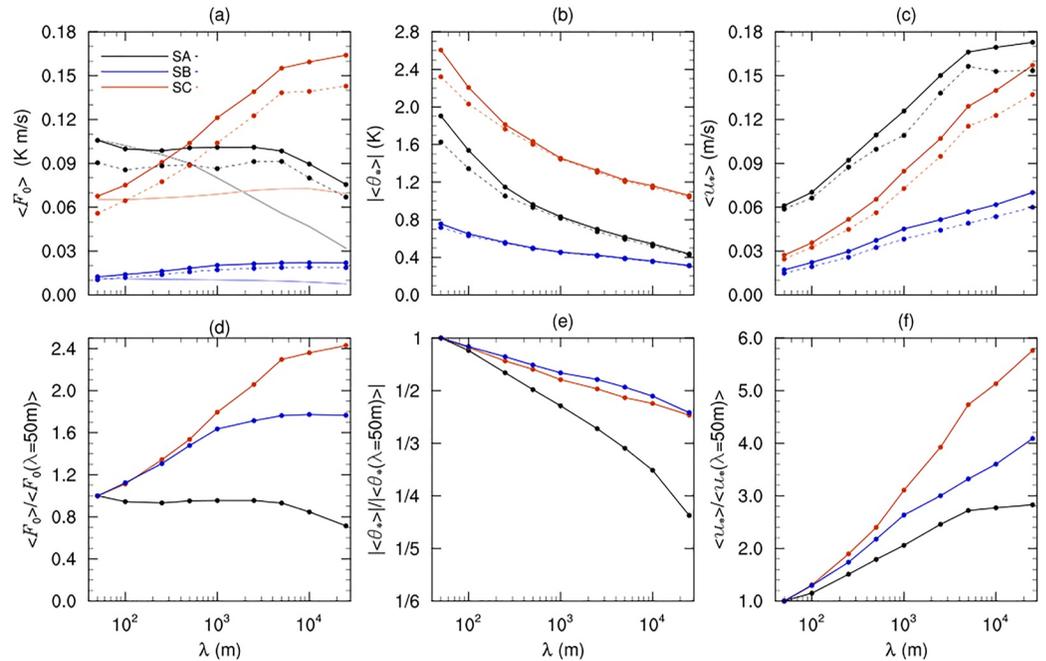
Figure 7. Lead-averaged surface heat flux (a), potential temperature scale (b) and friction velocity (c) as functions of lead width for SA, SB, and SC. (d)–(f) Show values normalized to the smallest lead, corresponding to (a)–(c), respectively. The dotted lines in (a)–(c) indicate the contributions of the forced convection regime of IBC. The light solid lines in (a) represent the heat flux in cases with a homogeneously heated surface (SA/SB/SC-10) as a function of analysis time for lead widths corresponding to SA, SB, and SC, and the abscissa represents $\tau(\lambda)$.

along lead width) and, consequently, to smaller values of $|\langle\theta_*\rangle|$. Another process that drives positive feedback is the ice-breeze velocity U_{ib}, which is defined here following Porson et al. (2007) for the sea breeze velocity:

$$U_{\text{ib}} = \frac{1}{Z_{\text{ib}}} \int_0^{Z_{\text{ib}}} \mathrm{d}z \, \langle u \rangle_y(z), \tag{5}$$

where Z_{ib} is the height at which $\langle u \rangle_y(z)$ reaches 0 for the first time. Integration is conducted at the left edge of the lead. Therefore, U_{ib} is a measure of the velocity of the lower branch of IBC directed toward the lead (compare with Figure 2b). Figure 8a shows that U_{ib} increases monotonically for all cases, for values between 0.1 and 0.3 m/s for the smallest leads and 1.2 and 2.7 m/s for the largest leads. From these results, we can conclude that the increase in friction velocity with increasing lead width is mainly controlled by the strength of IBC (IBC effect). The relative increase of U_{ib} is smallest for SA and largest for SC, coinciding with the relative increase of $\langle u_* \rangle$ for the corresponding cases (compare Figure 8b with Figure 7f). While Figure 7f implies that the relative increase of $\langle u_* \rangle$ depends on both ΔT_s and z_0 (because the values for SA, SB, and SC differ increasingly from each other with increasing lead width) Figure 7e indicates that the relative decrease of $|\langle\theta_*\rangle|$ depends mainly on z_0 (because the values for SB and SC are almost equal, while that for SA differs increasingly with increasing lead width from the others), considering the values for ΔT_s and z_0 in SA, SB, and SC (Table 1). In other words, the relative FDW effect is controlled by surface roughness rather than the temperature difference between water and ice, while the relative IBC effect is controlled by both factors.

To show that the forced convection regime of IBC is the main determinant of the lead-averaged surface heat flux, Figure 7a shows the contribution from IBC as dotted lines. In all cases and lead widths, IBC contributes more than 80% of the total flux. The contribution is calculated using Equation 3 within u_* and θ_* is calculated in the same manner as in the LES model, except that the mean values (averaged along y) of velocity, temperature, and the flux
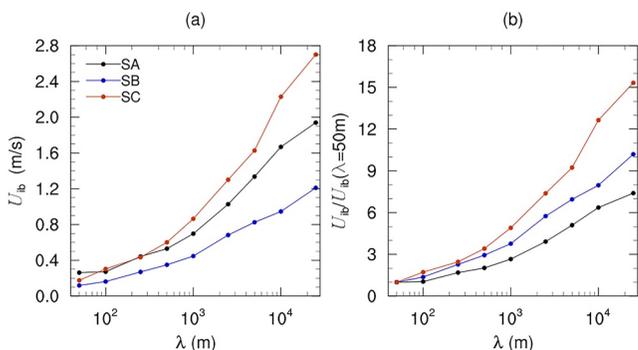

Figure 8. (a) Ice-breeze velocity as a function of lead width for SA, SB, and SC. (b) Same as (a) but normalized to the values for the smallest leads.

Richardson number are used for the calculation; for details, see Appendix A. The contributions to $|\langle\theta_*\rangle|$ and $\langle u_*\rangle$ of the mean values are represented in Figures 7b and 7c by dotted lines.

3.3. Does Heat Flux Converge Toward the Value for Homogeneous Heating With Increasing Lead Width?

For parameterization of lead-induced heat flux in (non-lead-resolving) weather and climate models, the question arises whether the parameterization of the water fraction for a location over the open ocean can be used. Therefore, in Figure 7a, the simulated surface heat flux of SA/SB/SC-10 (surface completely defined as water) is illustrated by light solid lines. Here, the abscissa corresponds to the analysis time $t = \tau(\lambda)$ of each case, SA, SB, and SC. Thus, the values for different lead widths can be compared with values for the open ocean over the same simulation time. The heat flux over a very large lead may be assumed to approach the value over open ocean, but our results show that it increasingly differs with increasing lead width. While for the smallest lead of $\lambda = 50$ m the values for each scenario almost identical to that for the open ocean at $t = \tau(\lambda = 50$ m), these values increasingly differ with larger lead width (and increasing $t = \tau(\lambda)$), reaching a difference of 2.5-fold between values for leads and the open ocean over the same time period. This difference is caused by permanent cold air advection driven by IBC over the lead, in contrast to the open ocean, where only free convection occurs. This cold air advection appears to be more efficient for wider leads, as illustrated by the increasing ice-breeze velocity (Figure 8). Notably, these conclusions only apply to conditions of weak background wind perpendicular to the lead. When significant background wind across the lead is present, IBC will be suppressed, and the heat flux may converge toward open-ocean conditions with increasing lead width.

3.4. Further Analysis of Plume Height and Scaling Laws

For parameterization of convection above leads in non-eddy-resolving microscale models, the plume height h is a key parameter (e.g., Lüpkes, Gryanik, et al., 2008; Lüpkes, Vihma, et al., 2008; Michaelis et al., 2020); therefore, h is briefly discussed here. Further, we examine an existing scaling law for the maximum plume height h_{max} and propose further scaling laws for the IBC.

We defined h as the height from the surface at which the vertical turbulent heat flux reaches its first minimum with a negative value. Figure 9a shows horizontal profiles of h for SC. From the ice edge, h first increases slightly, but at about $x/\lambda = \pm 0.1$ it begins to increase much more rapidly in all cases. At this position, the horizontal motion of the lower branch of IBC turns into upward motion. The maximum plume height h_{max} at the center of the lead varies from 150 m for the smallest lead to 750 m for the largest one. For all simulation chains (SA, SB, SC), h_{max} is shown as a function of lead width in Figure 9b, represented by crosses. Additionally, the dotted lines denote calculation results based on the scaling

$$h_{max} = \frac{c_1}{N}\left(\frac{g}{\theta_0}\langle F_0\rangle\lambda\right)^{1/3} \tag{6}$$

proposed by Zulauf and Krueger (2003) (with a slightly different notation adopted to match the notation of the present study). It was developed for conditions of lead-parallel background wind. Herein, θ_0 is a reference potential temperature, which we set to the value of near-surface temperature over ice, $N = \sqrt{g/\theta_0\partial_z\theta}$ the Brunt-Vaisala frequency, and $c_1 = 2.8$ is a proportionality constant. The value of c_1 was not explicitly provided by Zulauf and Krueger (2003), and we therefore determined it using values from Figure 10 of that study, wherein the scaling function for h_{max} is plotted against lead width for one case. Although c_1 was determined using values from a different case in another study, the scaling of h_{max} provided excellent results for all cases in our study, indicating that the value of c_1 may be universal. This is reinforced in Figure 9c, where the maximum plume heights based on LES are plotted against the corresponding values calculated using Equation 6. As reported by Zulauf and Krueger (2003), the difficulty lies in predicting lead-averaged surface heat flux, which was provided by the simulations in this study. In addition, we found that the height of the lower branch of the IBC Z_{ib} defined in Section 3.2 is proportional to h_{max}:

$$Z_{ib} = c_1' h_{max}, \tag{7}$$

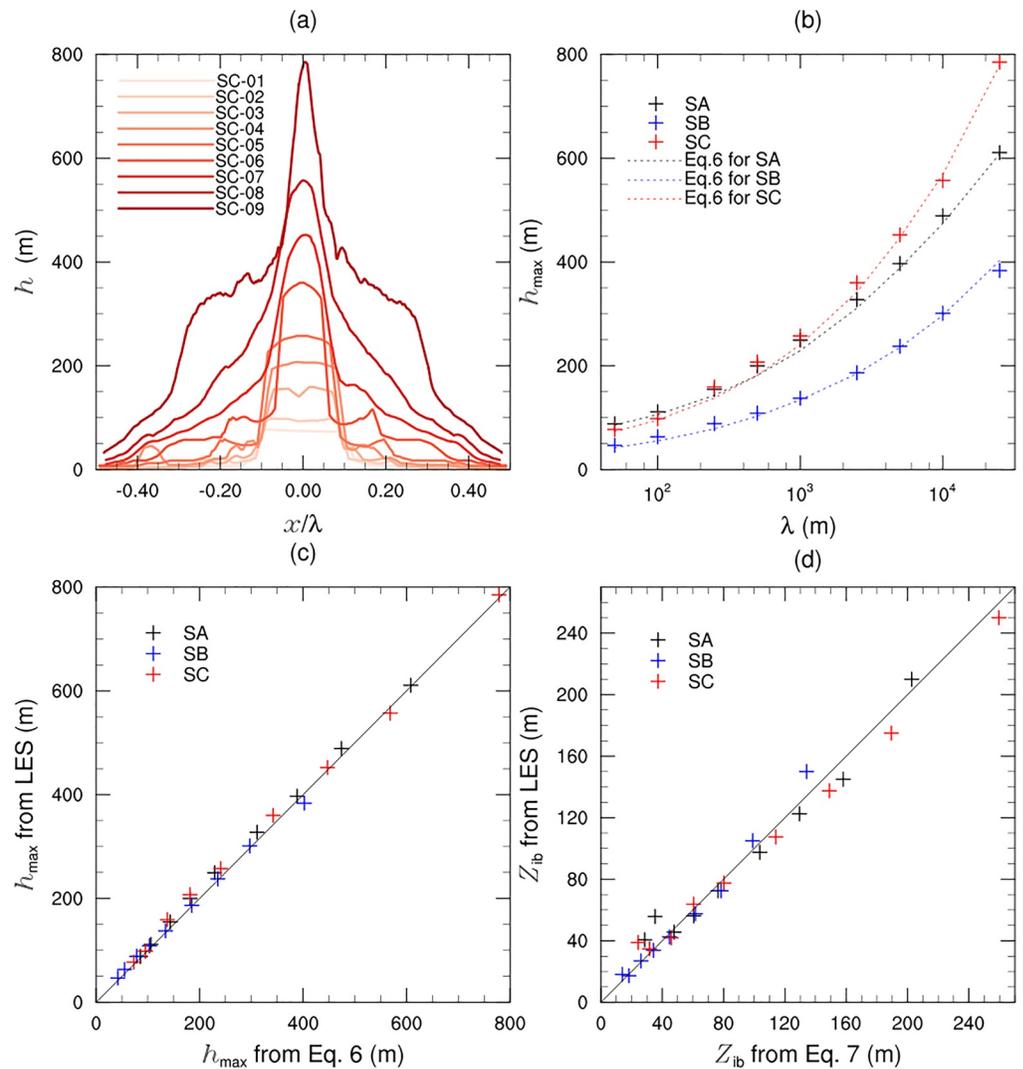**Figure 9.** (a) Horizontal profiles of plume height h for SC-01–SC-09 at $t = \tau$, (b) maximum plume height (h_{max}) as a function of λ for SA, SB, and SC at $t = \tau$ based on LES (crosses) and the calculation from Equation 6 (dotted lines), (c) and (d) maximum plume heights h_{max} and heights of the lower branch of IBC Z_{ib} based on LES (ordinate) versus their corresponding values calculated with Equations 6 and 7 (abscissa), respectively, for SA, SB, and SC at $t = \tau$.

with $c_1' = 0.33$. This is verified in Figure 9d, where Z_{ib} from LES is plotted against Z_{ib} from Equation 7, wherein h_{max} is determined by Equation 6.

Based on the surface buoyancy flux $\frac{g}{\theta_0}\langle F_0 \rangle$ and lead width λ and applying dimensional arguments, we propose two further scaling laws for the convection above leads without background wind (and possibly lead parallel background wind). The first is for the (horizontal) ice breeze velocity:

$$U_{ib} = c_2 \left(\frac{g}{\theta_0} \langle F_0 \rangle \lambda \right)^{1/3}. \tag{8}$$

The second is for the analysis time τ (time when the two branches of the IBC reaches the center of the lead) under the assumption it scales with the advective timescale λ/U_{ib}. Together with Equation 8 we obtain

$$\tau = c_3 \left(\frac{\lambda^2}{\frac{g}{\theta_0}\langle F_0 \rangle} \right)^{1/3}. \tag{9}$$
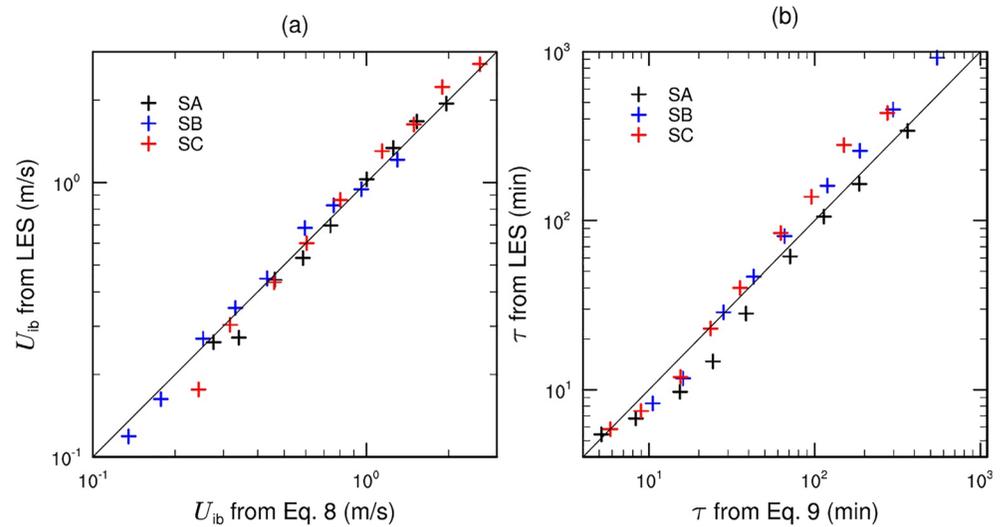
Figure 10. (a) Ice breeze velocity and (b) τ based on LES versus their corresponding values calculated using Equations 8 and 9 for SA, SB, and SC at $t = \tau$, respectively.

We determined the proportionality constants c_2 and c_3 with the data from SA, SB, and SC to be $c_2 = 0.475$ and $c_3 = 3.6$. The comparison of the values for U_{ib} and τ from Equations 8 to 9, respectively, versus LES data in Figure 10 confirms the scaling laws for the scenarios SA, SB, and SC.

We also tried to link the time τ into the context of the scaling laws for heterogeneously heated CBLs proposed by van Heerwaarden et al. (2014), who developed expressions describing the state of the CBL development in conjunction with the heterogeneity scale. However, applying the proposed timescale for the optimal state of the heterogeneous forcing (Equation 13 in van Heerwaarden et al. (2014)) to the problem of our study, did not yield in an appropriate scaling for τ. That might be due to the different setup of heterogeneity patterns. First, they were two-dimensional in van Heerwaarden et al. (2014) and one-dimensional in our study. Second, in van Heerwaarden et al. (2014) the patterns repeated periodically, while in our study the problem can be considered as non-periodic (up to a simulated time several times larger than τ). Although we support the idea of a universal scaling of surface heterogeneity, this indicates that future scalings need to be extended by further heterogeneity parameters.

Notably, in both our study and Zulauf and Krueger (2003), a stable stratified atmosphere with a constant vertical temperature gradient was initially defined. For conditions with nearly neutral stratification in the lowest few hundred meters capped by an inversion, which are often observed, the scaling laws from Equations 6 to 9 are unlikely to fit well.

3.5. Sensitivity to Coriolis Force

For comparability with ES07, the simulations presented up to this point were conducted without considering Coriolis force. The previous experiments in ES07 included two cases with Coriolis force, but ES07 found only marginal sensitivity of the convection over the lead to Coriolis effects (although in areas far from the lead, circulation shows branches with lead-parallel wind). ES07 expected low sensitivity due to the LES results of Mironov et al. (2000), who studied the effect of Coriolis force on convection. However, the conditions in Mironov et al. (2000) included homogeneous heating without background wind; therefore, a regime of purely free convection was investigated. Analysis of cases with broader leads in ES07 was conducted at a simulation time when IBC was not fully developed, as it had not reached the center of the lead (see Figure 6 in ES07); at that time, free convection presumably also dominated. As we discussed in Section 3.2, IBC has a major influence on surface heat flux and is a strong driver of convection. As IBC always reached the center of the lead in our analysis, the question arises whether the Coriolis force is an important factor. Calculation of the Rossby number

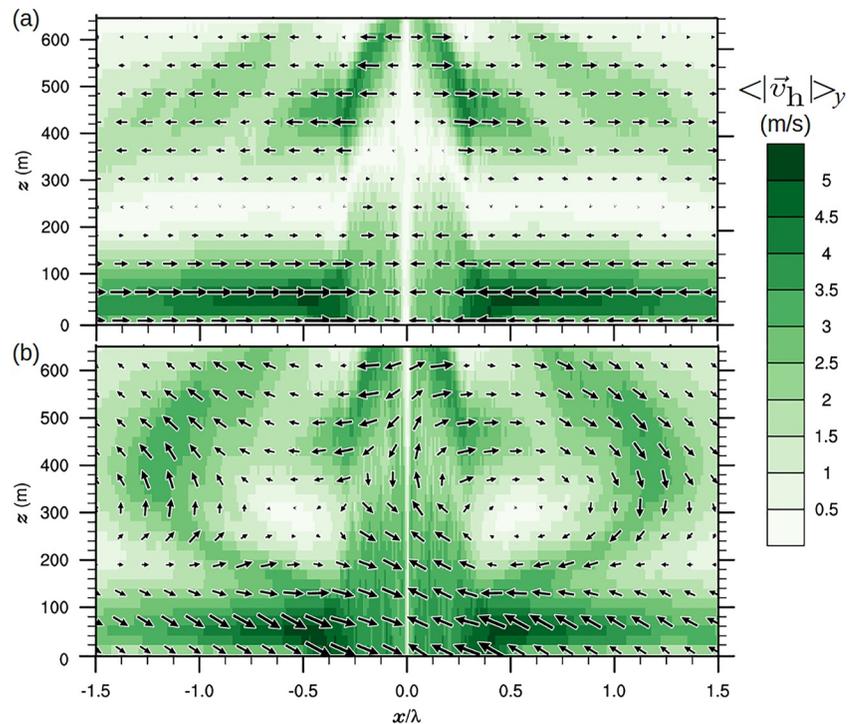$$\text{Ro} = \frac{U_{ib}}{\lambda f} \tag{10}$$

Figure 11. Vertical cross-sections of the horizontal wind vector (u, v) and absolute value of the horizontal wind speed averaged along y and over 900 s for a 25 km-wide lead (a) for scenarios SC without (SC-09) and (b) with Coriolis force (SC-09C) at $t = \tau$.

using U_{ib} from Figure 8 as the velocity scale and the Coriolis parameter of $f = 1.43 \times 10^{-4}\,\text{s}^{-1}$ at a latitude of 79° north gives values below 1 for $\lambda \geq 10$ km. In other words, the Coriolis force should have a strong influence on IBC for wide leads, which might feedback on convection. Figure 11 shows vertical cross-sections of horizontal winds (wind vector field $\vec{v}_h = (u, v)$ and absolute values $|\vec{v}_h|$) for SC-09 and SC-09C($\lambda = 25$ km) averaged along y and over 900 s. With the Coriolis force considered, the flow structure becomes much more complex. As reported by ES07, flow over ice becomes parallel to the lead, but only between the lower and upper branches of the circulation (between $z = 200$ and 400 m). Near-surface flow over the lead is slanted upward at 25° to the right of the corresponding flow direction without the Coriolis force. Thus, the fetch over the lead for near-surface winds increases with inclusion of the Coriolis force, which might explain why $\langle F_0 \rangle$ is increased by approximately 5% here (data not shown). For a 10 km-wide lead (data not shown), almost no difference was found in $\langle F_0 \rangle$ between SC-08 and SC-08C. Modification of the flow structure by the Coriolis force is similar, but less pronounced (i.e., only 10° deviation in the near-surface wind direction) than for smaller leads.

3.6. Sensitivity on Analysis Time τ

In Section 3.1.2, τ was defined as the time at which quasi-stationarity is reached, which coincidences with the time when the two branches of IBC merge at the center of the lead. As our analysis of the dependency of $\langle F_0 \rangle$ on lead width is based on that time, the sensitivity of these results to τ is discussed here. We concentrate solely on the cases of SB and SC, which have realistic roughness lengths. Figures 12a and 12b show these results for $t = 0.2$–2.0τ for SB and SC, respectively ($t = 0.2$–1.0τ is represented by solid lines, and $t = 1.0$–2.0τ by the red area). At $t = 0.2\tau$, the heat flux is nearly constant with lead width in both cases, with values similar to that obtained for the smallest lead at $t = \tau$. At this stage, the two branches of IBC have reached only the inner 10% of the lead; therefore, over more than 80% of the lead area, free convection dominates (see discussion in Section 3.1.1). This pattern is also evident from the small contribution, of approximately 10%–35%, of IBC to the total heat flux, which is indicated by the dotted lines. Over time, the heat flux and contribution of IBC increase, with wider leads showing larger increases. In the relatively long time interval from $t = \tau$–2.0τ (red shaded area), heat flux decreases slightly, that is, by less than 5%. Therefore, $t = \tau$ is an appropriate time for analysis.
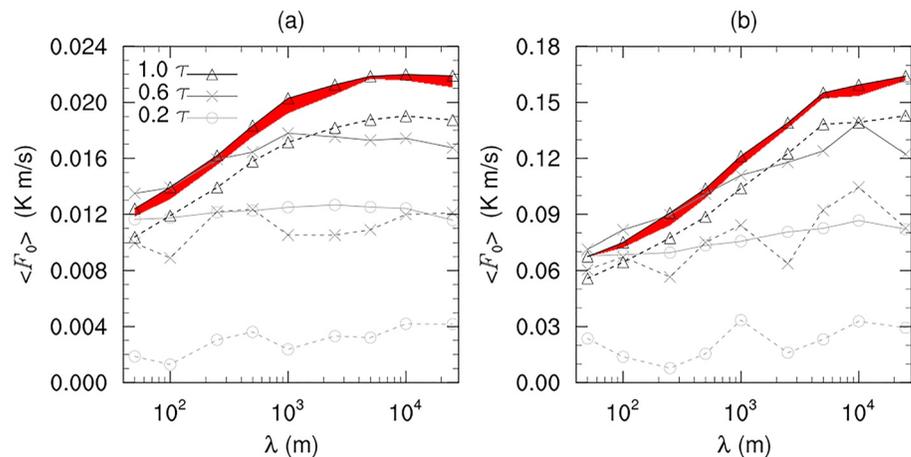
Figure 12. Lead-averaged surface heat flux $\langle F_0 \rangle$ as a function of lead width λ at various times between $t = 0.2$–2.0τ for (a) SB and (b) SC. The red area shows the range of results for times of $t = 1.0$–2.0τ. The dotted lines represent the contribution of IBC.

In nature, IBC is not always fully developed; therefore, fluxes obtained using parameterizations based on our results could be overestimated. However, we believe that, in most cases, IBC will be fully developed for the following reasons: first, for narrow leads on the order of 100 m and smaller, IBC develops within a few minutes (see Table 2). Second, wider leads develop from narrow leads through a growth process. During that growth process, we assume that the flow permanently adapts to the new lead width. This assumption requires further investigation.

4. Discussion and Conclusions

Using three series of LES, we investigated the dependency of lead-averaged surface heat flux on lead width under three different physical conditions (variations in near-surface temperature over ice and roughness length) without background wind. The first set of experiments SA used the same conditions as ES07, but the model resolution and domain differed. Analyzing the heat flux at the same fixed time as in ES07 ($t = 6$ hr) results qualitatively in a similar graph for the heat flux dependency on lead width (Figure 4) with a peak at $\lambda = 5$ km (in ES07 at $\lambda = 3$ km). But as our results in Sections 3.1.2 and 3.6 demonstrated, a fixed analysis time for this problem turns out not to be adequate. Using the individual time $t = \tau$ results in another shape of the heat flux against lead width (Figure 6). Now the largest fluxes appear for the smallest leads. While the effect of a single lead was investigated at a stage when the IBC was fully developed in SA (at $t = \tau$), the effect of multiple leads of the same width was assessed in ES07 (at $t = 6$ hr), and the developmental stage of IBC and ice-water fraction differed between these experiments. Although the results of ES07 must be interpreted with care, in the first LES parameter study for a wide range of lead widths, ES07 demonstrates the large impact of lead width on surface heat flux, and the importance of IBC.

The main result of SA, that is, that surface heat flux decreases with increasing lead width, is in agreement with previous parameterizations based on observations (e.g., Alam & Curry, 1997; Andreas & Cash, 1999). However, in experiments SB and SC, which had more realistic roughness lengths (two orders of magnitude smaller than in SA), heat flux increased significantly with increasing lead width. That discrepancy may be explained as follows: first, the cited parameterizations are based on measurements using leads smaller than a few hundred meters in width, while our study focused on wider leads. For very small leads, local processes such as ice topography may play a role, and we did not consider such effects. Second, our study focuses on conditions without background wind (zero geostrophic wind) but with a fully developed IBC. In contrast, the cited parameterizations presume the existence of background wind and the development of a continuous internal boundary layer from the upstream side of the lead edge to the downstream edge, in which IBC is completely suppressed.

Adjustment of the lead-averaged surface heat flux could be attributed mainly to two competing effects, namely the FDW effect causing negative feedback and IBC effect causing positive feedback. While the FDW effect was dominant in SA due to the (unrealistically) long roughness length, leading to a decrease in heat flux with increasing lead width, the IBC effect was dominant in SB and SC, leading to an increase in heat flux with increasing

lead width. Such competing effects were previously identified in the two-dimensional (non-eddy-resolving) study of Zulauf and Krueger (2003) with lead-parallel background wind, where similar IBCs appeared perpendicular to the mean wind, as in the present study. These effects were not discussed in detail, and were considered only for lead widths between 200 and 800 m. Generally, lead-averaged surface heat flux increased over the short span from the smallest to the widest lead, in accordance with our findings in SB and SC.

Zulauf and Krueger (2003) investigated the dependency of plume height on lead width and proposed a scaling law for it under conditions of lead-parallel wind. Applying this scaling to our cases, there was excellent agreement with the maximum plume heights obtained from our simulations. We proposed two further scaling laws for IBC, one for its horizontal velocity U_{ib} and one for the time τ when IBC is fully developed. Our LES data confirmed these scalings for all scenarios SA, SB, and SC.

For lead widths larger than 10 km, Coriolis force had a significant effect on the IBC flow structure. However, the lead-averaged surface heat flux differed slightly only for the widest simulated lead ($\lambda = 25$ km), reaching a value 5% greater than the corresponding result without consideration of the Coriolis force.

Although our results are valid only for conditions without background wind (which are rare in polar regions), they can be considered as a limiting case for conditions of weak background wind (perpendicular to the lead) in which IBC formation is not suppressed. The discussion of simulations with lead-parallel background wind in Zulauf and Krueger (2003) implies that our results apply qualitatively to such conditions.

Overall, the results of this study can be used to support the development of parameterization of near-surface heat flux over leads for non-lead-resolving models (e.g., Alam & Curry, 1997; Andreas & Cash, 1999) and of the convection above leads for non-turbulent-resolving (but lead-resolving) models (e.g., Lüpkes, Gryanik, et al., 2008; Lüpkes, Vihma, et al., 2008; Michaelis et al., 2020). Further studies of this type under more diverse meteorological conditions are needed, along with assessment of additional factors (e.g., background wind speed and direction, ice topography, lead opening and closing processes, different thermal stratification). Also, interaction effects between leads need to be investigated and the impact of spatially distributed leads of different size on the polar boundary layer. Studies of this kind are typically done using meso- or microscale (non-eddy-resolving) models (e.g., Dare & Atkinson, 2000; Michaelis & Lüpkes, 2022). As conventional parameterizations of convection have limitations concerning convection above leads (Lüpkes, Gryanik, et al., 2008; Lüpkes, Vihma, et al., 2008), improved parameterizations specialized for the lead problem are of significant importance for such studies. With increasing computer recourses, studies on the impact of spatially distributed leads of different sizes on the polar boundary layer will be increasingly feasible with LES-models. First efforts in that direction were done by Wenta and Herman (2018) with the Weather Research and Forecasting model in LES mode. Anyhow, in their simulations, the grid resolution of 100 m was rather coarse in relation to the considered lead widths between 200 and 1,000 m. As the resolution of an LES setup should be determined by the smallest lead considered, LES of situations with spatially distributed leads of different sizes are still challenging.

Appendix A: Calculation of the IBC Contribution to Surface Heat Flux

In our PALM model setup, surface heat flux is calculated using Equation 3, where u_* and θ_* are calculated following Monin–Obukhov similarity theory, which is assumed to be valid between the surface and the first vertical grid level (Maronga et al., 2020). Here, the vertical gradients of horizontal velocity $|\vec{v}_h|$ and potential temperature θ can be expressed in the unstable case as:

$$\partial_z |\vec{v}_h| = \frac{u_*}{\kappa z}\left(1 - 16\frac{z}{L}\right)^{-1/4} \tag{A1}$$

and

$$\partial_z \theta = \frac{\theta_*}{\kappa z}\left(1 - 16\frac{z}{L}\right)^{-1/2} \tag{A2}$$

where $\kappa = 0.4$ is the Karman constant and L is the Obukhov length. Integrating those equations between $z = z_0$ and the first vertical grid level $z = z_1$ gives:

$$u_* = \frac{\kappa |\vec{v}_h(z_1)|}{\ln\left(\frac{z_1}{z_0}\right) - \ln\left(\frac{(1+a_1)^2(1+a^2)}{(1+b_1)^2(1+b_1^2)}\right) + 2(\arctan(a_1) - \arctan(b_1))}, \tag{A3}$$

and

$$\theta_* = \frac{\kappa(\theta(z_1) - \theta(z_0))}{\ln\left(\frac{z_1}{z_0}\right) - 2\ln\left(\frac{1+a_2}{1+b_2}\right)},\tag{A4}$$

where $a_1 = (1 - 16z_1/L)^{1/4}$, $b_1 = (1 - 16z_0/L)^{1/4}$, $a_1 = (1 - 16z_1/L)^{1/2}$ and $b_1 = (1 - 16z_0/L)^{1/2}$. For the standard outputs of PALM, u_*, θ_* (and with Equation 3 accordingly F_0) and L are determined for each grid point and each time step. The contribution of the mean flow, namely IBC, was calculated in the same manner here using Equations A3, A4, and 3 during post-processing by replacing the local and instantaneous values for velocity, temperature and Obukhov length with their average values along y and over time. The temporal average varied between 100 s for the smallest leads and 900 s for the largest leads.

Data Availability Statement

We used PALM model system 21.10 (Maronga et al., 2015, 2020). Figures are plotted using NCL 6.6.2 (NCL, 2019). The PALM model source code, the steering file and user code for simulating the presented cases and NCL scripts for plotting and analyzing the model output data used for this study are available at https://doi.org/10.25835/jq6gctwq (Gryschka et al., 2022).

References

Alam, A., & Curry, J. A. (1997). Determination of surface turbulent fluxes over leads in Arctic sea ice. *Journal of Geophysical Research*, *102*(C2), 3331–3343. https://doi.org/10.1029/96JC03606

Andreas, E. L., & Cash, B. A. (1999). Convective heat transfer over wintertime leads and polynyas. *Journal of Geophysical Research*, *104*(C11), 25721–25734. https://doi.org/10.1029/1999JC900241

Andreas, E. L., & Murphy, B. (1986). Bulk transfer coefficients for heat and momentum over leads and polynyas. *Journal of Physical Oceanography*, *16*(11), 1875–1883. https://doi.org/10.1175/1520-0485(1986)016⟨1875:BTCFHA⟩2.0.CO;2

Andreas, E. L., Paulson, C. A., William, R. M., Lindsay, R. W., & Businger, J. A. (1979). The turbulent heat flux from Arctic leads. *Boundary-Layer Meteorology*, *17*(1), 57–91. https://doi.org/10.1007/BF00121937

Barry, R., Serreze, M., Maslanik, J., & Preller, R. (1993). The Arctic sea ice-climate system: Observations and modeling. *Reviews of Geophysics*, *31*(4), 397–422. https://doi.org/10.1029/93RG01998

Brutsaert, W. (1975). A theory for local evaporation (or heat transfer) from rough and smooth surfaces at ground level. *Water Resources Research*, *11*(4), 543–550. https://doi.org/10.1029/WR011i004p00543

Dare, R., & Atkinson, B. (2000). Atmospheric response to spatial variations in concentration and size of polynyas in the southern ocean sea-ice zone. *Boundary-Layer Meteorology*, *94*(1), 65–88. https://doi.org/10.1023/A:1002442212593

Deardorff, J. W. (1980). Stratocumulus-capped mixed layers derived from a three-dimensional model. *Boundary-Layer Leteorology*, *18*(4), 495–527. https://doi.org/10.1007/BF00119502

Eisen, O., & Kottmeier, C. (2000). On the importance of leads in sea ice to the energy balance and ice formation in the Weddell Sea. *Journal of Geophysical Research*, *105*(C6), 14045–14060. https://doi.org/10.1029/2000JC900050

Esau, I. N. (2007). Amplification of turbulent exchange over wide Arctic leads: Large-eddy simulation study. *Journal of Geophysical Research*, *112*(D8), D08109. https://doi.org/10.1029/2006JD007225

Glendening, J. W. (1995). Horizontally integrated atmospheric heat flux from an Arctic lead. *Journal of Geophysical Research*, *100*(C3), 4613–4620. https://doi.org/10.1029/94JC02424

Glendening, J. W., & Burk, S. D. (1992). Turbulent transport from an Arctic lead: A large-eddy simulation. *Boundary-Layer Meteorology*, *59*(4), 315–339. https://doi.org/10.1007/BF02215457

Grötzner, A., Sausen, R., & Claussen, M. (1996). The impact of sub-grid scale sea-ice inhomogeneities on the performance of the atmospheric general circulation model ECHAM3. *Climate Dynamics*, *12*(7), 477–496. https://doi.org/10.1007/s003820050122

Gryschka, M., Drüe, C., Etling, D., & Raasch, S. (2008). On the influence of sea-ice inhomogeneities onto roll convection in cold-air outbreaks. *Geophysical Research Letters*, *35*(23), L23804. https://doi.org/10.1029/2008GL035845

Gryschka, M., Fricke, J., & Raasch, S. (2014). On the impact of forced roll convection on vertical turbulent transport in cold air outbreaks. *Journal of Geophysical Research: Atmospheres*, *119*(22), 12–513. https://doi.org/10.1002/2014JD022160

Gryschka, M., Gryanik, V., Lüpkes, C., Mostafa, Z., Sühring, M., Witha, B., & Raasch, S. (2022). Data for "turbulent heat exchange over polar leads revisited: A large eddy simulation study" [Dataset]. https://doi.org/10.25835/jq6gctwq

Hanna, E. (1996). The role of Antarctic sea ice in global climate change. *Progress in Physical Geography*, *20*(4), 371–401. https://doi.org/10.1177/030913339602000401

Khanna, S., & Brasseur, J. G. (1998). Three-dimensional buoyancy-and shear-induced local structure of the atmospheric boundary layer. *Journal of the Atmospheric Sciences*, *55*(5), 710–743. https://doi.org/10.1175/1520-0469(1998)055⟨0710:TDBASI⟩2.0.CO;2

Ledley, T. S. (1988). A coupled energy balance climate-sea ice model: Impact of sea ice and leads on climate. *Journal of Geophysical Research*, *93*(D12), 15919–15932. https://doi.org/10.1029/JD093iD12p15919

Li, X., Krueger, S. K., Strong, C., & Mace, G. G. (2020). Relationship between wintertime leads and low clouds in the pan-arctic. *Journal of Geophysical Research: Atmospheres*, *125*(18), e2020JD032595. https://doi.org/10.1029/2020JD032595

Li, X., Krueger, S. K., Strong, C., Mace, G. G., & Benson, S. (2020). Midwinter arctic leads form and dissipate low clouds. *Nature Communications*, *11*(1), 206. https://doi.org/10.1038/s41467-019-14074-5

Lindsay, R., & Rothrock, D. (1995). Arctic sea ice leads from advanced very high resolution radiometer images. *Journal of Geophysical Research*, *100*(C3), 4533–4544. https://doi.org/10.1029/94JC02393

Lüpkes, C., Gryanik, V. M., Witha, B., Gryschka, M., Raasch, S., & Gollnik, T. (2008). Modeling convection over arctic leads with LES and a non-eddy-resolving microscale model. *Journal of Geophysical Research*, *113*(C9), C09028. https://doi.org/10.1029/2007JC004099

Lüpkes, C., Vihma, T., Birnbaum, G., & Wacker, U. (2008). Influence of leads in sea ice on the temperature of the atmospheric boundary layer during polar night. *Geophysical Research Letters*, *35*(3), L03805. https://doi.org/10.1029/2007GL032461

Marcq, S., & Weiss, J. (2012). Influence of sea ice lead-width distribution on turbulent heat transfer between the ocean and the atmosphere. *The Cryosphere*, *6*(1), 143–156. https://doi.org/10.5194/tc-6-143-2012

Maronga, B., Banzhaf, S., Burmeister, C., Esch, T., Forkel, R., Fröhlich, D., et al. (2020). Overview of the palm model system 6.0. *Geoscientific Model Development*, *13*(3), 1335–1372. https://doi.org/10.5194/gmd-13-1335-2020

Maronga, B., Gryschka, M., Heinze, R., Hoffmann, F., Kanani-Sühring, F., Keck, M., et al. (2015). The parallelized large-eddy simulation model (palm) version 4.0 for atmospheric and oceanic flows: Model formulation, recent developments, and future perspectives. *Geoscientific Model Development*, *8*(8), 2515–2551. https://doi.org/10.5194/gmd-8-2515-2015

Michaelis, J., & Lüpkes, C. (2022). The impact of lead patterns on mean profiles of wind, temperature, and turbulent fluxes in the atmospheric boundary layer over sea ice. *Atmosphere*, *13*(1), 148. https://doi.org/10.3390/atmos13010148

Michaelis, J., Lüpkes, C., Schmitt, A. U., & Hartmann, J. (2021). Modelling and parametrization of the convective flow over leads in sea ice and comparison with airborne observations. *Quarterly Journal of the Royal Meteorological Society*, *147*(735), 914–943. https://doi.org/10.1002/qj.3953

Michaelis, J., Lüpkes, C., Zhou, X., Gryschka, M., & Gryanik, V. M. (2020). Influence of lead width on the turbulent flow over sea ice leads: Modeling and parametrization. *Journal of Geophysical Research: Atmospheres*, *125*(15), e2019JD031996. https://doi.org/10.1029/2019JD031996

Midttun, L. (1985). Formation of dense bottom water in the Barents Sea. *Deep Sea Research Part A. Oceanographic Research Papers*, *32*(10), 1233–1241. https://doi.org/10.1016/0198-0149(85)90006-8

Miles, M. W., & Barry, R. G. (1998). A 5-year satellite climatology of winter sea ice leads in the western Arctic. *Journal of Geophysical Research*, *103*(C10), 21723–21734. https://doi.org/10.1029/98JC01997

Mironov, D., Gryanik, V. M., Moeng, C.-H., Olbers, D., & Warncke, T. (2000). Vertical turbulence structure and second-moment budgets in convection with rotation: A large-eddy simulation study. *Quarterly Journal of the Royal Meteorological Society*, *126*(563), 477–515. https://doi.org/10.1002/qj.49712656306

NCL. (2019). The NCAR command language (version 6.6.2) [Software]. UCAR/NCAR/CISL/TDD. https://doi.org/10.5065/D6WD3XH5

Porson, A., Steyn, D. G., & Schayes, G. (2007). Sea-breeze scaling from numerical model simulations, part I: Pure sea breezes. *Boundary-Layer Meteorology*, *122*(1), 17–29. https://doi.org/10.1007/s10546-006-9090-4

Ruffieux, D., Persson, P. O. G., Fairall, C., & Wolfe, D. E. (1995). Ice pack and lead surface energy budgets during LEADEX 1992. *Journal of Geophysical Research*, *100*(C3), 4593–4612. https://doi.org/10.1029/94JC02485

Salesky, S. T., Chamecki, M., & Bou-Zeid, E. (2017). On the nature of the transition between roll and cellular organization in the convective boundary layer. *Boundary-Layer Meteorology*, *163*(1), 41–68. https://doi.org/10.1007/s10546-016-0220-3

Serreze, M. C., Maslanik, J. A., Rehder, M. C., Schnell, R. C., Kahl, J. D., & Andreas, E. L. (1992). Theoretical heights of buoyant convection above open leads in the winter Arctic pack ice cover. *Journal of Geophysical Research*, *97*(C6), 9411–9422. https://doi.org/10.1029/92JC00688

Sühring, M., Maronga, B., Herbort, F., & Raasch, S. (2014). On the effect of surface heat-flux heterogeneities on the mixed-layer-top entrainment. *Boundary-Layer Meteorology*, *151*(3), 531–556. https://doi.org/10.1007/s10546-014-9913-7

Tetzlaff, A., Lüpkes, C., & Hartmann, J. (2015). Aircraft-based observations of atmospheric boundary-layer modification over arctic leads. *Quarterly Journal of the Royal Meteorological Society*, *141*(692), 2839–2856. https://doi.org/10.1002/qj.2568

Uttal, T., Curry, J. A., Mcphee, M. G., Perovich, D. K., Moritz, R. E., Maslanik, J. A., et al. (2002). Surface heat budget of the Arctic Ocean. *Bulletin of the American Meteorological Society*, *83*(2), 255–275. https://doi.org/10.1175/1520-0477(2002)083⟨0255:SHBOTA⟩2.3.CO;2

van Heerwaarden, C. C., Mellado, J. P., & De Lozar, A. (2014). Scaling laws for the heterogeneously heated free convective boundary layer. *Journal of the Atmospheric Sciences*, *71*(11), 3975–4000. https://doi.org/10.1175/JAS-D-13-0383.1

Wadhams, P., McLaren, A. S., & Weintraub, R. (1985). Ice thickness distribution in Davis Strait in February from submarine sonar profiles. *Journal of Geophysical Research*, *90*(C1), 1069–1077. https://doi.org/10.1029/JC090iC01p01069

Weinbrecht, S., & Raasch, S. (2001). High-resolution simulations of the turbulent flow in the vicinity of an Arctic lead. *Journal of Geophysical Research*, *106*(C11), 27035–27046. https://doi.org/10.1029/2000JC000781

Wenta, M., & Herman, A. (2018). The influence of the spatial distribution of leads and ice floes on the atmospheric boundary layer over fragmented sea ice. *Annals of Glaciology*, *59*(76pt2), 213–230. https://doi.org/10.1017/aog.2018.15

Wicker, L. J., & Skamarock, W. C. (2002). Time-splitting methods for elastic models using forward time schemes. *Monthly Weather Review*, *130*(8), 2088–2097. https://doi.org/10.1175/1520-0493(2002)130⟨2088:TSMFEM⟩2.0.CO;2

Williamson, J. H. (1980). Low-storage Runge-Kutta schemes. *Journal of Computational Physics*, *35*(1), 48–56. https://doi.org/10.1016/0021-9991(80)90033-9

Zulauf, M. A., & Krueger, S. K. (2003). Two-dimensional cloud-resolving modeling of the atmospheric effects of arctic leads based upon midwinter conditions at the surface heat budget of the Arctic Ocean ice camp. *Journal of Geophysical Research*, *108*(D10), 4312. https://doi.org/10.1029/2002JD002643